Earth and Planetary Science Letters 363 (2013) 50–60

Contents lists available at SciVerse ScienceDirect

Earth and Planetary Science Letters

journal homepage: www.elsevier.com/locate/epsl

Phase equilibria of ultramafic compositions on Mercury and the origin of the compositional dichotomy

Bernard Charlier *, Timothy L. Grove, Maria T. Zuber

Department of Earth, Atmospheric and Planetary Sciences, Massachusetts Institute of Technology, Cambridge, MA 02139, USA

ARTICLE INFO

Article history:
Received 10 May 2012
Received in revised form
11 December 2012
Accepted 13 December 2012
Editor: T. Spohn
Available online 20 January 2013

Keywords:
crustal composition
volcanism
MESSENGER
magma ocean
planetary formation

ABSTRACT

Measurements of major element ratios obtained by the MESSENGER spacecraft using x-ray fluorescence spectra are used to calculate absolute element abundances of lavas at the surface of Mercury. We discuss calculation methods and assumptions that take into account the distribution of major elements between silicate, metal, and sulfide components and the potential occurrence of sulfide minerals under reduced conditions. These first compositional data, which represent large areas of mixed high-reflectance volcanic plains and low-reflectance materials and do not include the northern volcanic plains, share common silica- and magnesium-rich characteristics. They are most similar to terrestrial volcanic rocks known as basaltic komatiites. Two compositional groups are distinguished by the presence or absence of a clinopyroxene component. Melting experiments at one atmosphere on the average compositions of each of the two groups constrain the potential mineralogy at Mercury's surface, which should be dominated by orthopyroxene (protoenstatite and orthoenstatite), plagioclase, minor olivine if any, clinopyroxene (augite), and tridymite. The two compositional groups cannot be related to each other by any fractional crystallization process, suggesting differentiated source compositions for the two components and implying multi-stage differentiation and remelting processes for Mercury. Comparison with high-pressure phase equilibria supports partial melting at pressure <10 kbar, in agreement with last equilibration of the melts close to the crust–mantle boundary with two different mantle lithologies (harzburgite and lherzolite). Magma ocean crystallization followed by adiabatic decompression of mantle layers during cumulate overturn and/or convection would have produced adequate conditions to explain surface compositions. The surface of Mercury is not an unmodified quenched crust of primordial bulk planetary composition. Ultramafic lavas from Mercury have high liquidus temperatures (1450–1350 °C) and very low viscosities, in accordance with the eruption style characterized by flooding of pre-existing impact craters by lava and absence of central volcanoes.

1. Introduction

Images of the surface of Mercury by Mariner 10 (e.g. Strom et al., 1975; Robinson and Lucey, 1997) revealed plains materials whose origin was debated, and not until additional, higher resolution images were acquired by the Mercury Surface, Space Environment, Geochemistry, and Ranging (MESSENGER) spacecraft did it become apparent that surface volcanism was widespread and produced kilometer-thick deposits (Head et al., 2008, 2011). Many pyroclastic deposits have also been identified (Rava and Hapke, 1987; Kerber et al., 2011). The crater deficiency of Mercury compared to the Moon even suggests that most of its surface has been volcanically resurfaced by intercrater plain emplacement (Fassett et al., 2011, 2012). Therefore, a substantial portion of the crust did certainly originate volcanically (Denevi et al., 2009). However, there are also some areas of Mercury that are heavily cratered and these might represent ancient surfaces, so that local preservation of a pristine upper crust cannot be completely ruled out. Surface rocks may thus represent a primary crust, possibly crystallized from a magma ocean (Brown and Elkins-Tanton, 2009), impact melts of superficial crustal materials, or products of partial melting of the planet's interior. Composition and origin of surface rocks thus provide a direct record of early planetary differentiation, crust and mantle formation, and evolution of these chemical reservoirs through time.

The first measurements of surface elemental abundance ratios by MESSENGER's X-Ray Spectrometer (XRS; Nittler et al., 2011) and the Gamma-Ray Spectrometer (GRS; Peplowski et al., 2011) produced surprises based on expectations and understanding of Mercury prior to the satellite's arrival. Some volatile elements (K and S) are not depleted and the low FeO content of the surface points to highly reduced conditions (Wadhwa, 2008; Malavergne

* Corresponding author. Tel.: +1 617 253 6398; fax: +1 617 253 7102.
E-mail addresses: charlier@mit.edu, b.charlier@ulg.ac.be (B. Charlier).

0012-821X/$ - see front matter © 2012 Elsevier B.V. All rights reserved.
http://dx.doi.org/10.1016/j.epsl.2012.12.021

et al., 2010; Zolotov, 2011; McCubbin et al., 2012). This suggests that chondritic materials are probably the building blocks of the planet, possibly either enstatite chondrite or bencubbinite (Wasson, 1988; Taylor and Scott, 2003; Malavergne et al., 2010).

In this study, XRS elemental ratios presented by Nittler et al. (2011) are used to calculate absolute abundances of major elements for surface materials. Data treated in this study do not include the northern volcanic plains described by Head et al. (2011). The ten XRS measurements discussed here have been acquired at high altitudes and thus cover large areas averaging the composition of various units (Fig. 1a), essentially a mixture of high-reflectance plains and a low-reflectance material (Head et al., 2008; Denevi et al., 2009). We discuss calculation methods and assumptions to take into account the speciation of major elements under reduced conditions relevant for Mercury. We evaluate the partitioning of major elements between silicate, metallic and sulfide melts and the nature and abundance of sulfide minerals at the surface of the planet. Calculated compositions are compared to terrestrial ultramafic compositions and the appropriate nomenclature for lavas on Mercury is presented. Two compositional groups have been identified and one-atmosphere melting experiments are presented for each average composition to constrain their emplacement temperature, crystallization paths and the potential mineralogy at the surface of Mercury. We also explore the physical properties of magmas on Mercury and discuss the implications of these compositional groups for the differentiation and melting processes on Mercury.

2. Surface compositions: calculations and assumptions

XRS measurements acquired during solar flares by MESSENGER allow detection of fluorescent signals of elements with atomic numbers up to that of Fe. The X-ray spectrum corresponds to the very surface with a maximum sampling depth of 100 μm. Elemental ratios for Mg/Si, Al/Si, S/Si, Ca/Si, Ti/Si and Fe/Si have been determined because ratios are largely independent of the measurement geometry and the total composition (Schlemm et al., 2007; Nittler et al., 2011).

Calculation of the absolute abundances from element ratios requires some assumptions. In silicate materials, major elements are usually considered to occur as oxides. However, under the reducing conditions that prevail on Mercury, estimated to be between 2.6 and 6.5 log units below the iron–wüstite buffer (Malavergne et al., 2010; Zolotov, 2011; McCubbin et al., 2012), iron occurs mainly as a metal phase or as a sulfide. Low- and high-pressure partial melting experiments at low fO_2 on the Indarch enstatite chondrite (McCoy et al., 1999; Berthet et al., 2009), a potential building block of Mercury (Wasson, 1988; Brown and Elkins-Tanton, 2009), have shown that immiscible metallic and sulfide melts are in equilibrium with the silicate melt. These iron and sulfide immiscible melts contain significant amounts of Si, Ca and Mg, showing that lithophile elements behave partly as siderophile and chalcophile elements under reducing conditions. The speciation of each element should thus be carefully evaluated before performing detailed interpretation of silicate melt compositions for Mercury.

2.1. Calculations on an oxide basis

The silicate part of the surface material of Mercury mainly contains the elements Si, Ti, Al, Fe, Mg, Ca and O. Consequently, element ratios relative to Si measured for these elements can be converted to oxides weight percent with a single possible solution when the total is normalized to 100% and oxygen is assumed to be the only anion. Alkalis (Na and K), manganese and phosphorous are first considered as minor elements in these MgO-rich compositions (see later for the potential effect of sodium). For example, MESSENGER's gamma-ray spectrometer measured an average of 0.28 ± 0.05 wt% K_2O in surface materials (Peplowski et al., 2011). This initial estimate considers only the silicate component of the XRS measurements. The effects of partitioning of Si, Fe, Ca and Mg between a silicate and immiscible metallic and sulfide melts are then considered and discussed.

Calculated compositions have low iron and titanium contents, from 0.6 to 4.9 wt% FeO and 0.3–1.3 wt% TiO_2 (Table 1). The low iron content confirms previous interpretations based on multispectral images (Blewett et al., 1997; McClintock et al., 2008) but the low titanium contents do not support a significant contribution by Ti-oxides in producing low-reflectance materials (Denevi et al., 2009; Riner et al., 2009, 2010, 2011; Sprague et al., 2009; Lawrence et al., 2010). The SiO_2 content is high and ranges from 52 to 60 wt%. Two compositional groups are distinguishable, mainly based on their calcium and aluminum contents (Fig. 1b). Group 1 (G1) has low Al_2O_3 (ca. 8 wt%), high CaO (10 wt%) and high MgO (25–27 wt%). Group 2 (G2) contains more Al_2O_3 (12–14 wt%), and less CaO (6–8 wt%) and lower MgO (18–23 wt%). Average compositions have been calculated for these two groups using XRS data that also include measurements for Ti/Si and Fe/Si ratios (Table 1).

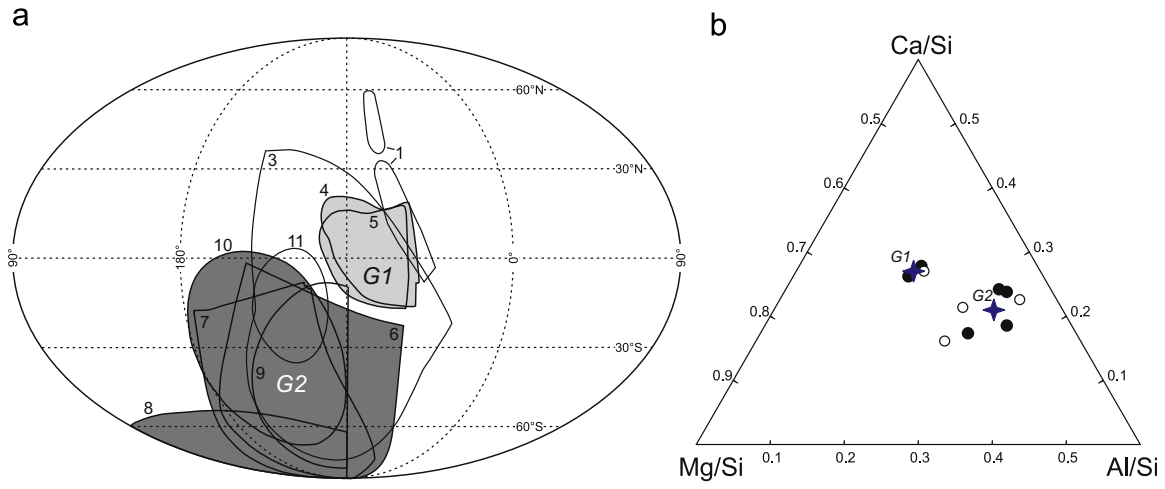

Fig. 1. XRS data from Nittler et al. (2011) for surface composition of Mercury. (a) Footprints sampled by XRS during measured solar flares, numbered according to Table 1. Light grey corresponds to the region for average composition G1 (data 4 and 5), dark grey is for average composition G2 (data 6, 7, 8 and 10). (b) Ternary diagram with Mg/Si, Ca/Si and Al/Si mass ratios. Black circles are data used to calculate average compositions (stars) for Group 1 (G1) and Group 2 (G2). White circles are data for which Fe/Si and Ti/Si were not acquired (data 1, 3, 9 and 11 of Table 1).

Table 1
Elemental ratios obtained for the surface of Mercury by XRS (Nittler et al., 2011), calculated absolute abundances and average compositions used in the experimental study.

	1	3	4	5	6	7	8	9	10	11	G1[c]	G2[d]
Elemental ratios measured by XRS (Nittler et al., 2011)[a]												
Mg/Si	0.62	0.50	0.58	0.67	0.41	0.43	0.39	0.36	0.53	0.64	0.63	0.44
Al/Si	0.19	0.24	0.17	0.18	0.25	0.28	0.26	0.26	0.27	0.28	0.18	0.27
S/Si	0.14	0.09	0.15	0.15	0.07	0.07	0.05	0.06	0.07	0.07	0.15	0.07
Ca/Si	0.30	0.20	0.29	0.30	0.21	0.22	0.15	0.18	0.17	0.18	0.30	0.19
Ti/Si[b]			< 0.01	0.010	0.007	0.03	0.007		< 0.01			
Fe/Si			0.03	0.06	0.12	0.15	0.05		0.08		0.05	0.10
Oxide basis (wt%) normalized to 100 wt% without sulfur												
SiO_2	54.2	57.8	55.1	52.1	57.0	54.4	60.0	61.5	55.1	53.7	53.6	56.6
Al_2O_3	9.10	12.3	8.27	8.29	12.6	13.5	13.8	14.1	13.1	13.3	8.28	13.2
MgO	26.1	22.4	24.8	27.1	18.1	18.1	18.1	17.2	22.6	26.7	25.9	19.3
CaO	10.6	7.56	10.4	10.2	7.83	7.83	5.89	7.24	6.12	6.33	10.3	6.92
FeO			0.99	1.88	4.12	4.91	1.81		2.65		1.44	3.37
TiO_2			0.43	0.41	0.31	1.27	0.33		0.43		0.42	0.59
η (Pa s)[h]	1.0	3.7	1.5	0.8	4.7	3.3	8.4	12.7	2.1	1.2	1.1	4.0
CIPW norm calculation (wt%)												
Quartz		9.1	1.6		11.0	7.9	19.1	20.3	6.4	0.3		10.6
Plagioclase	24.8	33.6	22.6	22.6	34.4	36.8	29.2	35.9	30.4	31.4	22.6	34.3
Diopside	21.6	3.1	22.6	21.9	3.5	1.6					22.3	
Hypersthene	50.2	54.4	52.4	41.9	50.5	51.3	47.9	42.8	60.5	66.5	50.0	53.3
Olivine	3.3			12.8							4.3	
Ilmenite			0.8	0.8	0.6	2.4	0.6		0.8		0.8	1.1
Corundum							3.1	0.9	2.0	1.8		0.6
Sulfur content based on normalization to 100 wt% oxides+sulfur												
S	3.43	2.37	3.72	3.53	1.83	1.75	1.38	1.70	1.77	1.73	3.63	1.68
Recalculation after elements partitioning between silicate, sulfide and iron melts and extra S as $(Ca_{0.5},Mg_{0.5})S$												
SiO_2			58.5	55.5	60.4	57.9	61.9		57.5		57.0	59.5
Al_2O_3			8.78	8.82	13.4	14.5	14.2		13.8		8.80	14.0
MgO			23.8	26.5	18.1	18.4	17.9		22.5		25.1	19.2
CaO			8.45	8.77	7.73	7.84	5.62		5.73		8.61	6.71
TiO_2			0.46	0.43	0.33	1.37	0.34		0.45		0.44	0.62
Sulfide melt[e]			2.58	4.87	4.58	4.38	3.45		4.43		3.72	4.21
Iron melt[f]			0.00	0.00	2.03	2.78	0.41		0.81		0.00	1.51
$(Ca_{0.5},Mg_{0.5})S$			5.39	3.17	0.00	0.00	0.00		0.00		4.28	0.00
η (Pa s)[h]			2.7	1.3	10.4	7.3	13.5		3.4		1.9	7.6
CIPW norm calculation (wt%) without TiO_2[g]												
Quartz			8.8	1.4	17.2	13.7	23.2		11.7		5.2	16.5
Plagioclase			24.0	24.0	36.6	38.9	27.9		28.4		24.0	33.3
Diopside			14.0	15.1	1.4						14.6	
Hypersthene			52.8	59.0	44.4	45.8	44.6		56.0		55.8	47.8
Corundum						0.3	4.0		3.4			1.8

[a] Composition 2 from Nittler et al. (2011) was not used because Ca/Si has not been measured.
[b] Values for Ti/Si < 0.01 have been considered equal to 0.01.
[c] G1 is the average of compositions 4 and 5.
[d] G2 is the average of compositions 6, 7, 8 and 10.
[e] Sulfide melt calculated with 40 (wt%) S, 30 (wt%) Fe, 15 (wt%) Ca and 15 (wt%) Mg.
[f] Iron melt calculated with 90 (wt%) Fe and 10 (wt%) Si.
[g] CIPW norms with TiO_2 calculate a titanite component.
[h] Viscosity of the silicate melt calculated at 1450 (°C) for G1 compositions and 1380 (°C) for G2 compositions using Giordano et al. (2008).

The normative mineralogy recalculated from XRS measurements converted to wt% of oxides (Table 1) predicts that Group 1 consists essentially of orthopyroxene (50 wt%), clinopyroxene (22 wt%), plagioclase (23 wt%) and minor olivine (4 wt%). Group 2 contains orthopyroxene (53 wt%), plagioclase (34 wt%) and quartz (11 wt%). The minor corundum component in this group can be accounted for by the incorporation of Al_2O_3 in orthopyroxene. Using an oxide basis for all elements, these two compositional groups are thus separated by the quartz saturation plane (i.e. olivine-bearing versus quartz-bearing compositions), and Group 2 is notably devoid of clinopyroxene.

2.2. The roles of sulfur and iron metal

Ratios of S/Si are high, which points to significant amounts of sulfur at the surface of Mercury (Nittler et al., 2011). Calculated S abundances range from 1.4 to 3.7 wt% S (Table 1). The sulfur content of surface compositions shows a clear correlation with calcium and aluminum (Fig. 2a–b). Correlation between sulfur and magnesium is not obvious although, on average, Mg-rich compositions have a higher S content (Fig. 2c). The link between Ca, Mg and S suggests the potential occurrence of oldhamite (CaS) and niningerite (MgS) or a solid solution between these two end-members ((Ca,Mg)S), common phases in enstatite chondrites (e.g. Keil, 1968; Larimer and Ganapathy, 1987). The correlation between Ca and S has been further corroborated by more recent data (Weider et al., 2012).

Rocks at the surface of Mercury are mostly lavas in which sulfides could occur as multicomponent immiscible sulfide melt blebs. Element partitioning between silicate–metal–sulfide immiscible melts is strongly dependent on equilibrium conditions, particularly pressure, temperature and oxygen fugacity. The lithophile, siderophile and chalcophile behavior of elements

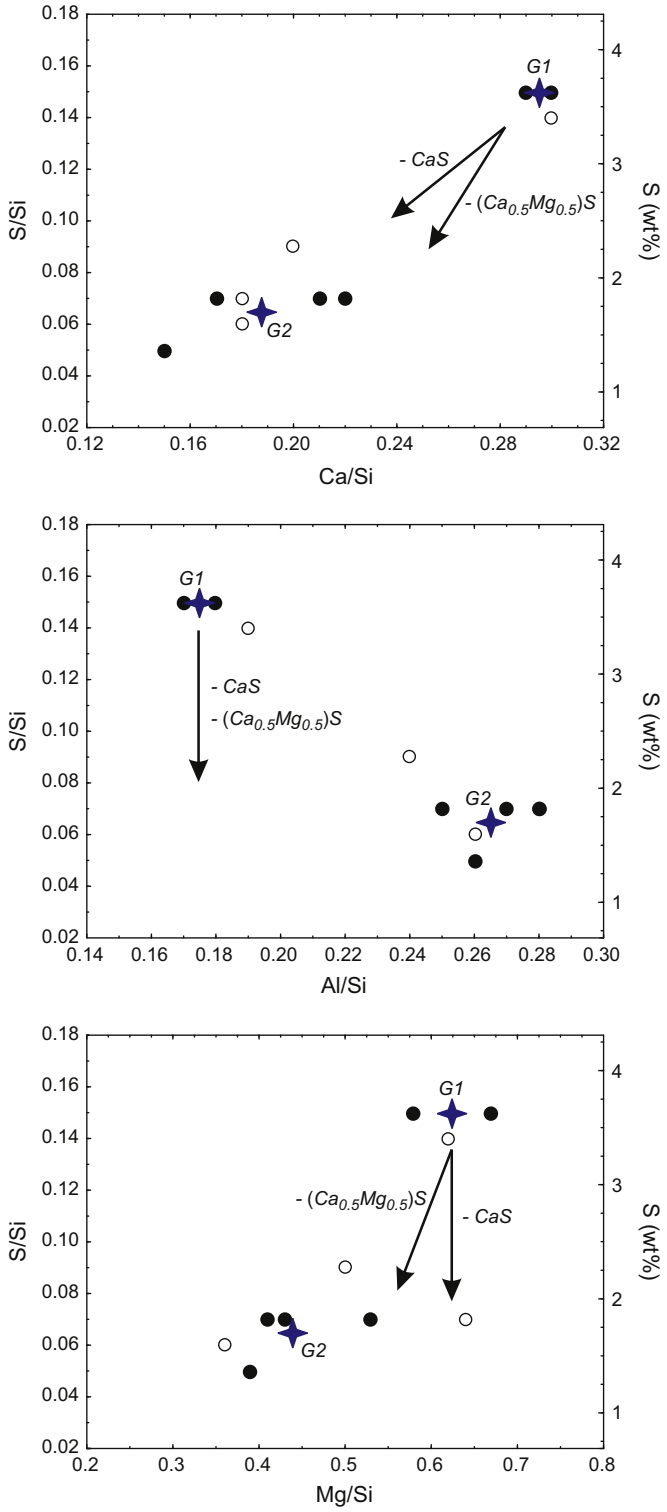

Fig. 2. XRS data from Nittler et al. (2011) for surface composition of Mercury plotted for S/Si as a function of Ca/Si, Al/Si and Mg/Si mass ratios. The sulfur content expressed as weight percent on the *Y* axis is calculated using the linear regression between S/Si and S (wt%) based on normalization to 100 wt% oxides + sulfur ($r^2 = 0.994$). Black circles are data used to calculate average compositions (stars) for Group 1 (G1) and Group 2 (G2). White circles are data for which Fe/Si and Ti/Si were not acquired. Arrows are vectors indicating the compositional shift after subtraction of CaS and $(Ca_{0.5}Mg_{0.5})S$.

changes with temperature, pressure and oxygen fugacity conditions (e.g. Li and Agee, 1996; Corgne et al., 2008; Berthet et al., 2009). Melting experiments performed at ambient pressure and reduced conditions on the Indarch enstatite chondrite by McCoy et al. (1999) are presently the best available proxy for understanding element partitioning between silicate–metal–sulfide immiscible melts under high-temperature reduced conditions assumed to prevail during the emplacement of lavas at the surface of Mercury. In the temperature range 1200–1450 °C relevant for magnesium-rich compositions, a Fe–Ni–Si-rich metal liquid develops and contains up to 7.7 wt% Si and 85–90 wt% Fe (McCoy et al., 1999). Another phosphorous-bearing metal melt is present and contains a maximum of 3 wt% Si at 1450 °C. The immiscible sulfide melt in these experiments is dominated by Fe (26–38 wt% Fe) and S (37–42 wt% S), and contains up to 12 wt% Ca and 12 wt% Mg.

These data allow us to infer the actual silicate melt composition by taking into account the partitioning of major elements between immiscible silicate, metal and sulfide melts in the bulk composition measured by XRS (Nittler et al., 2011). We use the most conservative approach with high concentrations of lithophile elements in the sulfide and metal melts (sulfide melt with 40 wt% S, 30 wt% Fe, 15 wt% Ca and 15 wt% Mg; metal melt with 90 wt% Fe and 10 wt% Si). We first assign S completely to the sulfide melt; Fe is then attributed to the sulfide melt and any remaining Fe is attributed to metal melt. Iron in the high bulk S/Fe compositions 4 and 5 of Nittler et al. (2011) (see Table 1) is completely partitioned into the sulfide melt. Iron metal is thus absent. The excess S is then attributed to a sulfide phase with the composition $(Ca_{0.5}Mg_{0.5})S$. Results for these calculations are presented in Table 1.

The recalculated compositions for the silicate melt are only slightly different from those calculated on an oxide basis (Fig. 3). SiO_2 and Al_2O_3 are slightly higher; MgO and CaO are slightly lower, particularly in S-rich samples (Group 1). Calculations show that normative olivine is now absent from all compositions. The gap between the two compositional groups is slightly reduced, but large differences remain. Normative calculations (Table 1) suggest that clinopyroxene is still relatively abundant in Group 1 (15 wt%) and absent from Group 2. Both groups have normative quartz, which is more abundant in Group 2 (17 versus 5 wt% on average). The hypersthene/plagioclase ratio is higher in Group 1 (2.3 versus 1.4). The presence of immiscible iron metal instead of FeO dissolved in the silicate melt would not have any effect on the discrimination between two compositional groups.

The occurrence of pure oldhamite (CaS) at the surface would explain the composition gap for CaO between the two groups. The vector showing the effect of CaS removal from bulk surface compositions is displayed in Fig. 2. However, removal of this mineral from the high-Ca, high-S group does not account for the gap in Al/Si, or for the higher average Mg/Si of compositions from Group 1. Subtraction of $(Ca_{0.5}Mg_{0.5})S$ would better relate the two groups for the Mg content, but the trend for Ca deviates and the gap for Al is still not explained. Consequently, the presence of a clinopyroxene component still distinguishes the two groups. Moreover, at reducing conditions, S also combines with Cr and Mn (McCoy et al., 1999), two elements that might have been identified on spectra acquired during intense solar flares (Nittler, pers. com.). Our calculations to correct the effect of sulfides on Ca and Mg concentrations in the silicate melt are thus probably the most conservative.

2.3. The role of sodium

Evans et al. (2012) have reported a first average abundance estimate of ca. 2.9 wt% Na (3.9 wt% Na_2O) on Mercury's surface. This presence of Na in lavas from Mercury would produce albite component, which is Si-enriched compared to anorthite. Consequently, the silica component of the non-albite fraction would be lower and the compositions would contain more olivine. However,

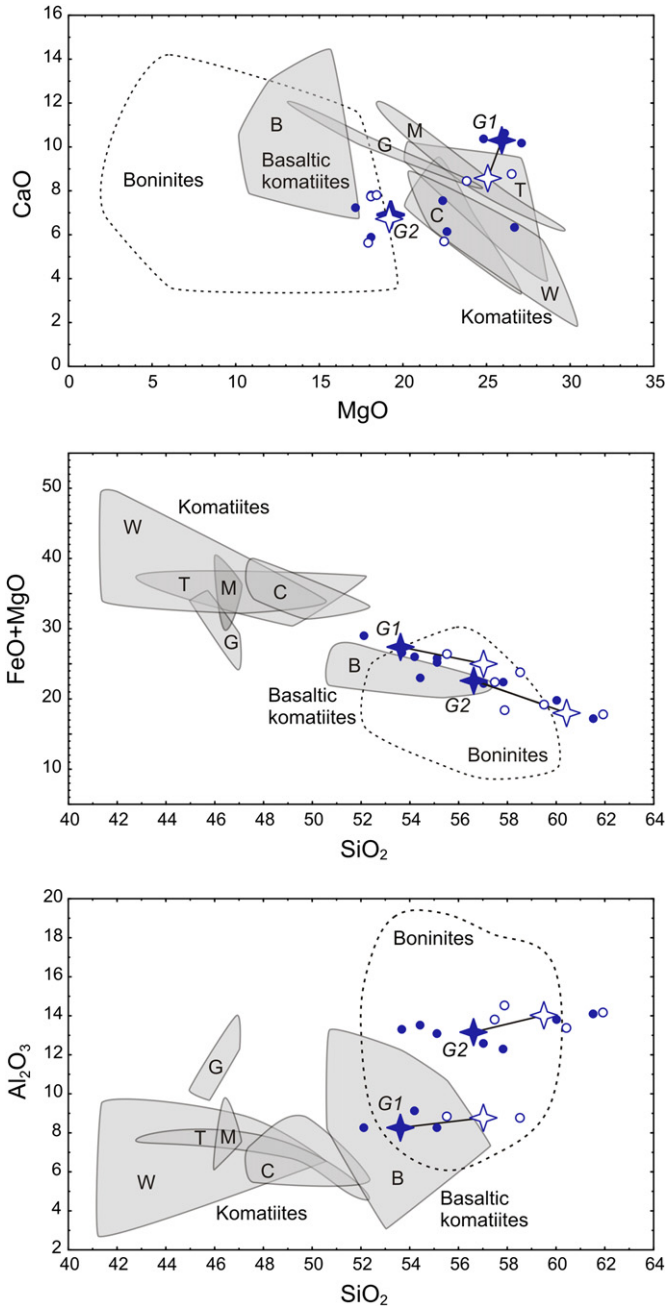

Fig. 3. Comparison between the composition of terrestrial ultramafic lavas and surface compositions of Mercury. Komatiites compositions from Gorgona, Colombia (G; Aitken and Echeverría, 1984); Wawa, Superior Province, Canada (W; Polat et al., 1999); Tisdale and Munro, Abitibi (T and M; Fan and Kerrich, 1997); North Caribou greenstone belt, Superior Province (C; Hollings and Kerrich, 1999); basaltic komatiites from Barbeton (B; Parman et al., 2001); Boninites data from Georoc database filtered to 52 wt% $> SiO_2 <$ 60 wt%; MgO $<$ 20 wt%; n=369. Filled symbols are data calculated on an oxide basis; white symbols are data corrected for the distribution of major elements between silicate, metal and sulfide melts.

Na does not have any effect on the compositional dichotomy. The main implication is that plagioclase would be more albitic and more abundant, and the olivine/orthopyroxene ratio would be higher. Spatially-resolved data for Na are needed to make progress on this issue.

2.4. Nomenclature for lavas on Mercury

Lavas at the surface of Mercury are characterized by high MgO. This suggests a similarity to the high-temperature ultramafic komatiites emplaced on Earth, mainly during the Proterozoic and Archean (Arndt and Nisbet, 1982; de Wit and Ashwal, 1997; Grove and Parman, 2004). Komatiites are defined as lavas with $<$52 wt% SiO_2, $>$18 wt% MgO and $<$1 wt% TiO_2, and contain spinifex olivine textures (Le Bas, 2000). Komatiites are commonly associated with basaltic komatiites, a term introduced by Viljoen and Viljoen (1969) for rocks with lower MgO and higher SiO_2 contents. These lavas are nevertheless more refractory (more MgO-rich) compared to boninites, defined as containing $>$52 wt% SiO_2 and $>$8 wt% MgO (Le Bas, 2000). On Earth, high MgO ultramafic lavas also contain a significant amount of iron, usually 9–13 wt% FeO_{tot} in komatiites and basaltic komatiites, and 7–10 wt% FeO_{tot} in boninites.

The compositions of lavas from Mercury display MgO contents in the range of komatiites (17–28 wt% MgO; Fig. 3a). However, they contain much lower iron so that FeO_{tot}+MgO is close to that of basaltic komatiites and boninites (Fig. 3b). Silica is also distinctively higher in the Mercury ultramafic rocks compared to komatiites, and encompasses the range of basaltic komatiites and even higher (Fig. 3c). The rocks at the surface of Mercury which have been measured by XRS (Nittler et al., 2011) are probably closest in composition to basaltic komatiites and should be referred to as such.

3. Experiments: goals and methods

Low-pressure melting experiments have been conducted on average compositions for Groups 1 and 2 estimated using the recalculated oxide basis. The objectives of these experiments are to determine liquidus temperatures, identify the location and cotectic/peritectic character of the olivine/low-Ca pyroxene boundary curve (i.e. the limit between the stability fields of the two phases) and recognize the details of low-Ca pyroxene phase relations (protoenstatite, orthoenstatite and pigeonite). Experiments were conducted along the quartz–fayalite–magnetite buffer, so that iron is mainly present as FeO in the silicate melt. Comparing these data with phase equilibria in the CaO–MgO–Al_2O_3–SiO_2 (CMAS) simplified system (Andersen, 1915; Osborn and Tait, 1952; Kushiro, 1972; Presnall et al., 1978, 1979; Longhi and Boudreau, 1980; Sen and Presnall, 1984; Liu and Presnall, 1990) allows us to constrain the phase relations for the entire plausible range of Mg-number of lavas that might be present on the surface of Mercury. At the high Mg-numbers represented in the Mercury and CMAS compositions, the low-Ca pyroxene stability fields along the olivine liquidus surface are protoenstatite, followed by orthoenstatite and then pigeonite (Longhi and Pan, 1988).

Starting compositions were prepared by mixing high-purity oxides and silicates. We used SiO_2, TiO_2, Al_2O_3, MgO, and $CaSiO_3$ in the appropriate proportions. Iron was added as Fe_2O_3 and Fe metal sponge in stoichiometric proportions to produce FeO. The reagents were mixed under ethanol in an agate mortar for 5 h. The Fe sponge was then added to the mixture and ground for an additional 1 h. The mixtures were then conditioned at one atmosphere pressure in a DelTech vertical gas-mixing furnace for 48 h at an oxygen fugacity corresponding to the QFM buffer at 1100 °C.

Experiments at one atmosphere were performed at MIT in vertical-tube DelTech quenching furnaces, with a CO_2–H_2 gas atmosphere. The oxygen fugacity was monitored using a ZrO_2–CaO oxygen cell and was kept near the QFM buffer. The sample material for these experiments consisted of ca. 50 mg of the oxide mixture mixed with polyvinyl alcohol as a binder. The pellet was prepared onto an iron–platinum alloy loop, which had been previously annealed with 4–5 wt% Fe to prevent Fe loss to the alloy during the experiment (Grove, 1981). The sample temperature was measured using a Pt–$Pt_{90}Rh_{10}$ thermocouple calibrated to the melting points of NaCl, Au, and Pd. The thermocouple was placed in the

hotspot of the furnace, where the thermal gradient is <1 °C/cm. The sample was suspended alongside the thermocouple, so they were at the same level within the furnace. The temperature reproducibility of this arrangement is better than 5 °C. Isothermal experiments were performed. The sample was held in the hotspot of the furnace and the temperature was increased to the target, equilibrating for 5–90h. All samples were drop-quenched into water.

Compositions of the minerals and glasses were analyzed using wavelength dispersive spectrometry on the 5-spectrometer JEOL 8200 electron microprobe at MIT. Natural and synthetic primary and secondary standards were used, and the CITZAF online data correction package was used for all analyses (Armstrong, 1995). Mineral analyses were performed with a 15 kV accelerating voltage and a beam current of 10 nA, utilizing a focused beam spot. Glass compositions were measured using a 10 μm defocused beam, 10 nA beam current, and 15 kV accelerating voltage.

4. Experimental results

The phase relations and run conditions for starting compositions G1 and G2 are reported in Supplementary Table 1. Composition G1 crystallizes olivine as the liquidus mineral at 1440 °C. It is followed by protoenstatite at 1322 °C, easily identified because it inverts to clinoenstatite upon quenching and develops cracks (Fig. 4; Smith, 1969). This phenomenon is also observed in natural rocks, e.g. in boninites and chondrites (Yasuda et al., 1983). Orthoenstatite, free of cracks and slightly more CaO-rich compared to protoenstatite (2.0–3.0 versus 0.7–0.8 wt% CaO), starts crystallizing at 1300 °C. Augite appears at 1250 °C. Plagioclase has been observed at 1200 °C but the composition of the melt in this experiment close to the solidus could not be measured. Composition G2 is slightly quartz normative and is located in the protoenstatite stability field which crystallizes as the liquidus phase at 1350 °C. Orthoenstatite follows at 1224 °C and plagioclase and quartz appear together on the liquidus at 1200 °C. Composition G2 does not crystallize clinopyroxene. The pigeonite stability field has not been encountered in our experiments (Longhi and Boudreau, 1980). Olivine produced from composition G1 contains 1.1–1.9 wt% FeO (Fo_{98-99}). Protoenstatite contains 0.8–1.0 wt% FeO in experiments G1, and 2.0–4.1 wt% FeO in experiments G2.

The compositional evolution of parent melts (compositions G1 and G2) with temperature is illustrated in Fig. 5. In the investigated range of temperatures, the fraction of residual liquid in the experiments is broadly higher than 40–50%. Liquids we produced thus correspond to the first stages of crystallization under equilibrium conditions. The variation of SiO_2 content with crystallization is low, certainly below the resolution that could be achieved by XRS measurements at the surface of Mercury. MgO

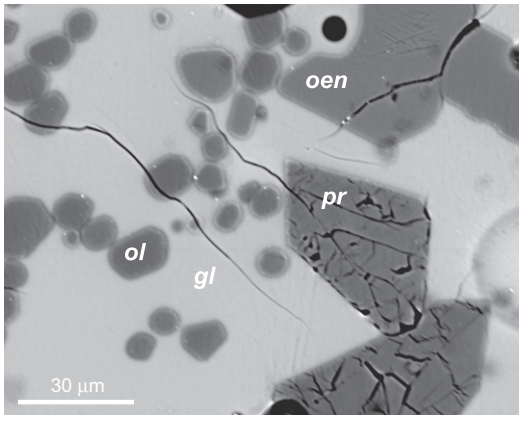

Fig. 4. Back-scattered electron images of products from experiment G1–5 (1300 °C). *gl* quenched glass; *ol* olivine; *oen* orthoenstatite; *pr* protoenstatite.

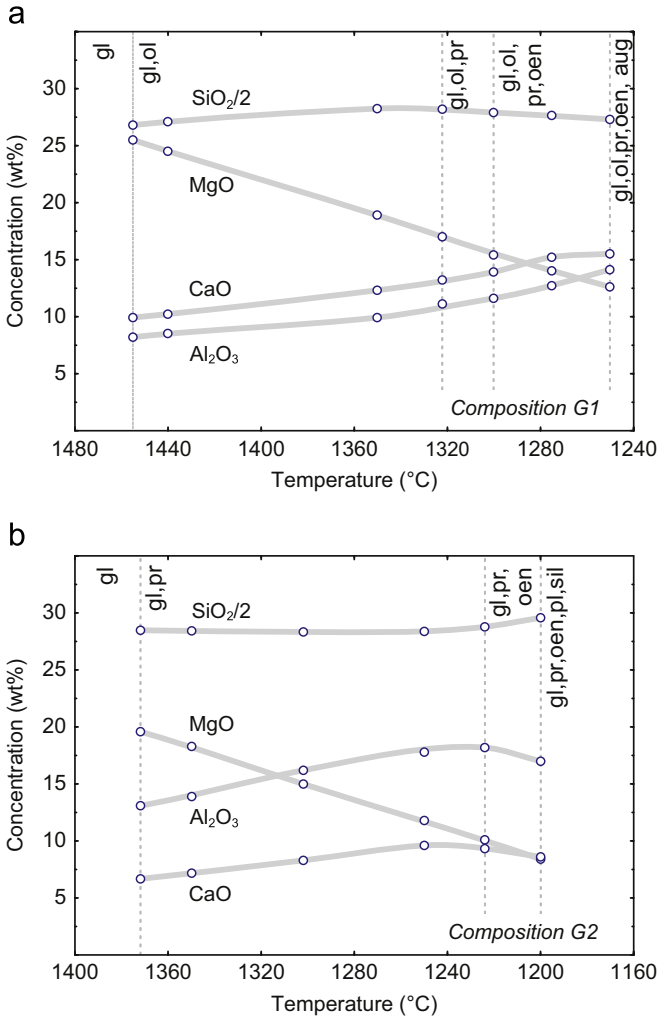

Fig. 5. Concentration of major elements in experimental glasses as a function of temperature for (a) starting composition G1; and (b) starting composition G2. Vertical dashed lines mark the appearance of a new liquidus phase. *gl* quenched glass; *ol* olivine; *oen* orthoenstatite; *pr* protoenstatite; *aug* augite; *pl* plagioclase; *sil* silica phase.

decreases continuously with differentiation, approximately by a factor 2–3 in a 200 °C crystallization interval. Al_2O_3 and CaO increase with decreasing temperature, as both elements are moderately incompatible in early crystallizing phases (olivine and low-Ca pyroxenes). The concentration of these two elements starts decreasing in composition G2 when plagioclase becomes a stable crystallizing phase, probably slightly before 1200 °C.

Under the reducing conditions of Mercury, it is probable that liquidus temperatures might be slightly different, mainly because of the absence of Fe^{2+} in the melt. However, Gudfinnsson and Presnall (2000) have shown experimentally that isobarically, for every 1 wt% increase in the FeO content of the melt in equilibrium with the lherzolite phase assemblage, the equilibrium temperature is lower by about 3–5 °C. Consequently, because the compositions G1 and G2 have respectively 1.4 and 3.4 wt% FeO, the effect of this element on the liquidus temperature is minor.

5. Discussion

5.1. Low-pressure differentiation of Mercury lavas

The experimentally produced liquids at 1-atm are projected into the Olivine–Clinopyroxene–Quartz, Olivine–Clinopyroxene–Anorthite

and Olivine–Anorthite–Quartz sub-projections of the Olivine–Clinopyroxene–Anorthite–Quartz pseudo-quaternary system (Fig. 6). These sub-projections clearly show the different crystallization paths followed by the two surface composition groups. The presence of a clinopyroxene component in Group 1 and its absence in Group 2 are responsible for contrasting evolution with differentiation. During cooling, G1 will ultimately crystallize clinopyroxene while G2 will not. Consequently, the two compositional groups cannot be related to each other by any differentiation process due to cooling and crystallization at low pressure. This conclusion is also valid if crystallization under high-pressure occurred. Indeed, because G1 has a higher liquidus temperature than G2, the only way to relate both compositions by fractional crystallization is to subtract clinopyroxene from G1 as the sole phase. Even if the stability field of clinopyroxene expands with pressure, the experimental study of Weng and Presnall (2001) in the system Diopside–Forsterite–Enstatite clearly shows that early crystallization of clinopyroxene as the first liquidus phase is impossible for composition G1 under any P–T conditions relevant for Mercury. This suggests that these lavas are derived from different source materials, supporting the notion that the silicate portion of Mercury is differentiated.

The crystallization paths of compositions calculated on an oxide basis and those corrected for the presence of metal and sulfide melts, and sulfides minerals are not drastically different. The major difference is observed for G1. While G1 calculated on an oxide basis crystallizes a significant amount of olivine before reaching the saturation with protoenstatite (ca. 18 wt%; Supplementary Table 1), the corrected G1 composition is much closer to the olivine–protoenstatite peritectic and will crystallize small amounts of olivine if any. Neither G2 composition crystallizes olivine at all. We can conclude from this that, compared to ultramafic compositions on Earth, lavas on Mercury crystallize much less olivine and are dominated by the early crystallization of pyroxenes (protoenstatite and orthoenstatite).

XRS measurements cover large areas because they have been acquired at high altitudes (Fig. 1a). Here, we discuss crystallization paths for average compositions and do not consider individual measurements, or analytical uncertainties reported by Nittler et al. (2011). This assumption is justified by the small size of the compositional variations within groups G1 and G2. Even if some small compositional scattering in group G2 might be responsible for a range of liquidus temperatures and for variable proportions of solid phases at the solidus, the nature of solid phases and their order of crystallization will be the same in the group.

The presence of Na in ultramafic lavas would have some implications for low-pressure phase equilibria. First, this element reduces the liquidus temperature. The high average amount of Na (3.9 wt% Na_2O) reported by Evans et al. (2012) would also produce significantly different calculated mineral component. As illustrated in Fig. 6 for corrected average compositions G1 and G2, Na-bearing compositions have lower Quartz component and higher Plagioclase and Olivine components. G1 and G2 compositions would thus crystallize higher amount of olivine and plagioclase.

5.2. Comparison with high-pressure phase equilibria

The G1 and G2 compositions are compared to the saturation boundaries determined in this study and in the CMAS system (Presnall et al., 1979; Sen and Presnall, 1984; Liu and Presnall, 1990) at elevated pressure (Fig. 7). The small amount of Fe in the Mercury compositions does not have much effect on the location of the phase boundaries in these projections, and allows us to compare our low-pressure data to the published high pressure phase relations. The G1 composition calculated on an oxide basis lies on the olivine–low-Ca pyroxene (proto- or ortho-enstatite) boundary curve at ca. 10 kbar and the G1 composition corrected for metal and sulfide lies on the 1-atm olivine–protoenstatite peritectic (Fig. 7a). The significance of the proximity of this composition to these saturation boundaries is that G1 could represent lavas produced by partial melting of an olivine–low-Ca

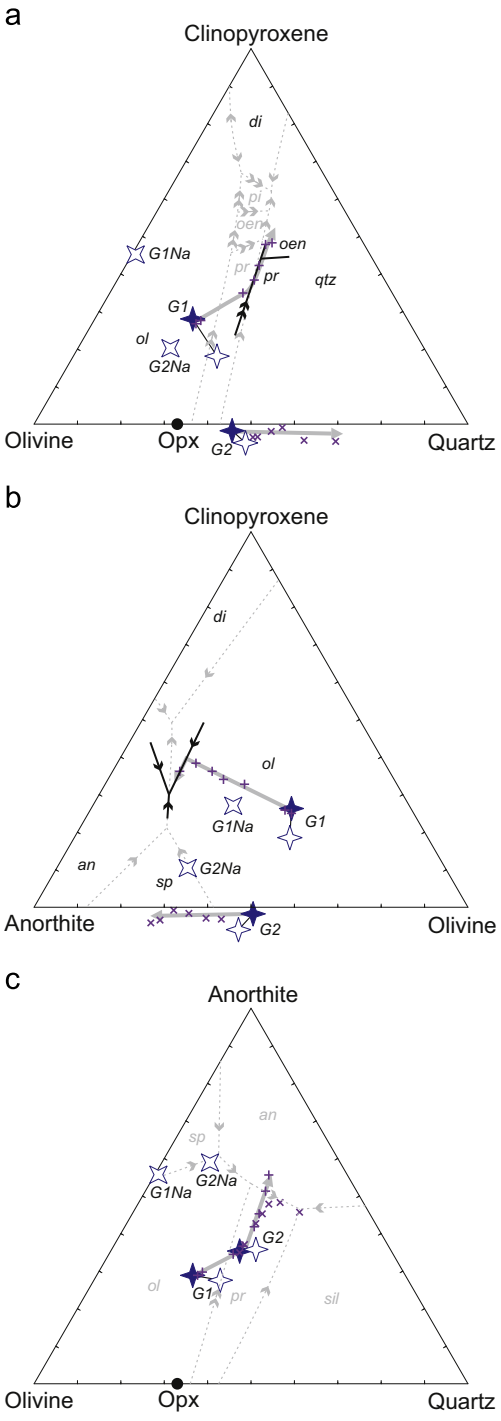

Fig. 6. Projection of experimental liquids on pseudo-ternary liquidus section. (a) Projection from anorthite onto the plane olivine, clinopyroxene and quartz; (b) projection from quartz onto the plane anorthite, olivine and clinopyroxene; and (c) projection from clinopyroxene onto the plane olivine, anorthite and quartz. Dashed grey liquidus boundaries are from data in ternary systems involving forsterite, diopside, silica and anorthosite compiled from Andersen (1915), Osborn and Tait (1952), Kushiro (1972) and Longhi and Boudreau (1980). Filled symbols are data calculated on an oxide basis; white symbols are data corrected for the distribution of major elements between silicate, metal and sulfide melts. G1Na and G2Na are corrected compositions with 3.9 wt% Na_2O. Normalization into components in oxygen units after Grove (1993).

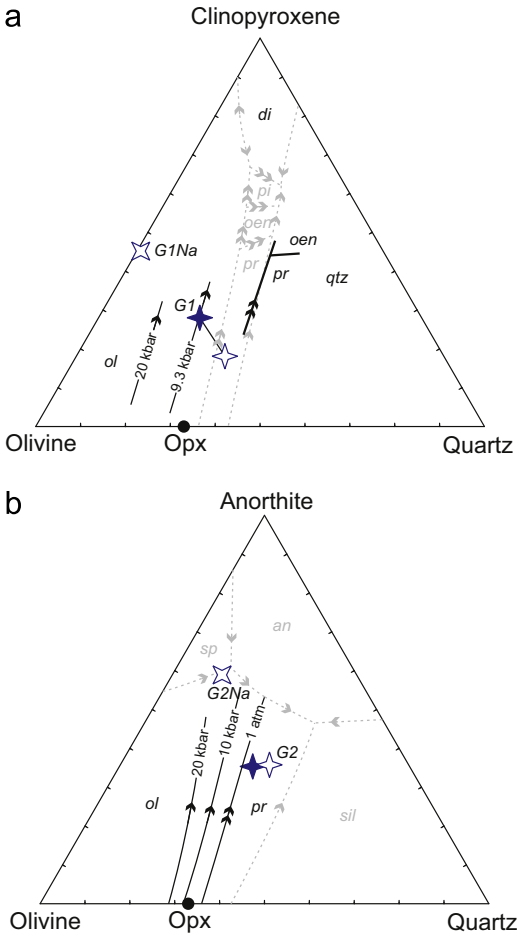

Fig. 7. Comparisons between low-pressure and high-pressure phase equilibria. (a) Projection from anorthite onto plane olivine, clinopyroxene and quartz. High-pressure boundary curves are from Presnall et al. (1979). (b) Projection from clinopyroxene onto plane olivine, anorthite and quartz. High-pressure boundary curves are from Sen and Presnall (1984) and Liu and Presnall (1990). Dashed grey low-pressure liquidus boundaries are from data in ternary systems involving forsterite, diopside, silica and anorthosite compiled from Andersen (1915), Osborn and Tait (1952), Kushiro (1972) and Longhi and Boudreau (1980). Filled symbols are data calculated on an oxide basis; white symbols are data corrected for the distribution of major elements between silicate, metal and sulfide melts. G1Na and G2Na are corrected compositions with 3.9 wt% Na_2O. The saturation boundaries at 1 atm in the high Mg-number Mercury bulk compositions coincide with those of CMAS allowing a meaningful comparison with the CMAS data in these projection schemes. Normalization into components in oxygen units after Grove (1993).

pyroxene–clinopyroxene–anorthite bearing source region at low pressure (<10 kbar). Alternatively, the G1 composition could be a residual liquid produced by shallow crystallization processes at low pressure (<10 kbar). The parental melt could have been generated by melting at higher pressures and/or by higher extents of melting and would be enriched in olivine component and more komatiitic compared to G1.

The G2 composition calculated on an oxide basis and the G2 composition corrected for metal and sulfide need to be examined in a different pseudo-ternary system, because they do not contain clinopyroxene. When these two compositions are plotted in the Olivine–Anorthite–Quartz pseudo-ternary (Fig. 7b), both lie in the 1-atm protoenstatite liquidus volume near the olivine–protoenstatite peritectic. The significance of this composition and its relation to these low-pressure boundaries is that G2 could represent a partial melt of an orthopyroxene–plagioclase–quartz-bearing source region. In this situation the source region would be dominantly orthopyroxene-bearing and the degree of melting would have to be high. The depth conditions for this melting process are difficult to constrain because of the high orthopyroxene content of the melt, but low pressures (<10 kbar) cannot be ruled out. Alternatively, the G2 composition could be a residual liquid produced by shallow crystallization processes at low pressures (<10 kbar) of a liquid derived from an olivine–low-Ca pyroxene–anorthite bearing source. These phase equilibrium constraints will be used to discuss models for the origin of the two crustal compositional types. Note that if significant amounts of Na were present on Mercury, both G1 and G2 compositions would become more olivine normative. Producing these ultramafic lavas would then require partial melting of deeper sources.

5.3. Physical properties of lavas and eruption style on Mercury

Chemical and thermal characteristics of lavas at the surface of Mercury have direct implications for the dynamics of eruption and lava flows. While some pyroclastic deposits have been emplaced during explosive eruption due to decompression and expansion of volatiles (Kerber et al., 2011), most eruptions have formed plains with broad, thick flow fronts (Head et al., 2011). Calculations of viscosities (Giordano et al., 2008) for surface lavas at the liquidus temperature, 1450 °C for Group 1 and 1380 °C for Group 2, range from 0.8 to 13.5 Pa s which is at the lower limit of any silicate melt measured (Table 1). This property is an important characteristic of these lava compositions and is consistent with the low viscosity emplacement styles observed on Mercury, fast and voluminous flooding of magma at the surface of the planet and absence of large volcanoes (Head et al., 2011).

5.4. Compositional variation and terrains on Mercury

The surface of Mercury has low Al/Si and Ca/Si ratios and thus does not contain a plagioclase-rich crust similar to anorthositic highlands on the Moon (Nittler et al., 2011). The silica content is higher than any 'basaltic' compositions on the Moon and Mars (Fig. 8). This is consistent with the high SiO_2 contents that have been proposed for potential compositions of the bulk silicate fraction of Mercury (Supplementary Table 2). However, the surface data reported by Nittler et al. (2011) do not correspond to any bulk planetary silicate compositions. This supports the idea that the silicate portion of Mercury has been differentiated.

Various geological terrains have been identified based on color variations related to compositional heterogeneities correlated with morphological features (Robinson and Lucey, 1997; Robinson et al., 2008; Denevi et al., 2009). Intercrater plains have high abundances of primary and secondary craters and are interpreted to be emplaced during the Late Heavy Bombardment. Smooth plains are less cratered and have sharp morphological boundaries (Head et al., 2008). Such a large continuous flood occurs at high northern latitudes and covers ca. 6% of the planet and this is most likely a young volcanic deposit. Similar high-reflectance material is recognized elsewhere on the planet within craters and basins, particularly associated with the Caloris basin (Denevi et al., 2009). These areas have ages near the end of the Late Heavy Bombardment (3.7–3.8 Ga; Head et al., 2011) and may have a volcanic origin, while some might represent impact melts and/or basin ejecta (Denevi et al., 2009). Recent volcanism, possibly as young as 1 Ga, has been identified near the Rachmaninoff basin, suggesting prolonged duration of volcanic activity on Mercury (Prockter et al., 2010). Finally, low-reflectance material covers more than 15% of the planet and may represent a lower crustal component (Robinson et al., 2008; Denevi et al., 2009). It has diffuse limits with surrounding materials and is usually exhibited in large craters and basins, suggesting a deeper origin.

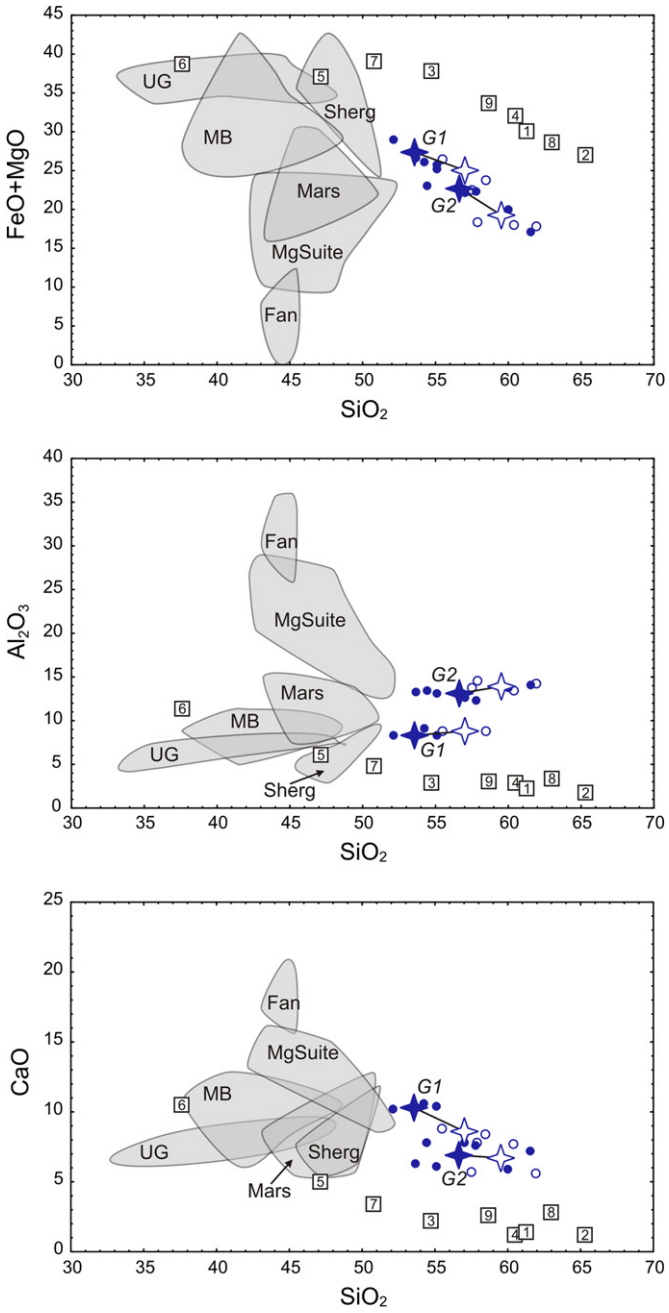

Fig. 8. Comparison of the composition of lavas at the surface of Mercury with ferroan lunar anorthosites (Fan), lunar magnesian-suite (MgSuite), lunar mare basalts (MB; data compiled in Papike et al., 1998), lunar ultramafic glasses (UM; Delano, 1986), surface basalts from Mars (Mars), shergottites (Sherg; data compiled by Filiberto and Dasgupta, 2011) and potential compositions of the bulk silicate fraction of Mercury (numbers refer to Supplementary Table 2). Filled symbols are data calculated on an oxide basis; white symbols are data corrected for the distribution of major elements between silicate, metal and sulfide melts.

Data discussed in this study essentially cover mixed areas of high-reflectance plains and a low-reflectance material (Head et al., 2008; Denevi et al., 2009). Identifying the relative contribution of each terrain is currently not possible, but higher spatial resolution measurements will help understanding the origin of the two compositional groups. With the compositional data discussed in this study, there are some fundamental principles that must hold if partial melting of a planetary interior and/or differentiation of a silicate magma ocean led to the observed chemical differences in these compositional types. These constraints on melting/crystallization are used to discuss models for the origin of Mercury presented in the following section.

New data published by Weider et al. (2012) expand the database of Nittler et al. (2011). Interestingly, Weider et al. (2012) still identify two clusters of data points for the older terrain (excluding the Northern plains). The dataset also extends to compositions with higher Mg/Si up to 0.8 compared to 0.6 in Nittler et al. (2011). These compositions would be closer to komatiites with 33 wt% MgO, 51 wt% SiO_2, 4–6 wt% Al_2O_3 and 6–8 wt% CaO. Our G2 composition is also close to data for the Northern plains although it has slightly higher Mg/Si (0.44 for G2 compared to 0.34 on average for the Northern plains).

5.5. Origin of compositional variations of surface terrains on Mercury

The compositional information from these initial measurements can be used to evaluate several models for planetary accretion and differentiation of Mercury. The compositions of the Mercurian crust are plotted in Fig. 8 along with planetary mafic and ultramafic magma compositions and proposed Mercury bulk silicate mantle compositions (see Supplementary Table 2). It is clear that none of the crustal compositions is close to what would be expected if there was a quenched crust on Mercury that would have preserved a primordial composition from an early magma ocean. The two compositions are products of solid/melt differentiation processes.

Near fractional melting is one magmatic process that could allow the two compositions G1 and G2 to be related. An olivine–low-Ca pyroxene–clinopyroxene–anorthite source mantle must be subjected to fractional melting where the melt was extracted from the solid residue as it was produced until all the clinopyroxene was exhausted. Melting then ceases and starts again only when the temperature has increased to the higher temperature of the olivine–low-Ca pyroxene–anorthite saturation boundary in the clinopyroxene-free sub-system (e.g. Yoder, 1976, pp. 107–109). However, such a process is not consistent with liquidus temperature for the G1 and G2 compositions. For such a fractional melting process to work, G1 should have a lower liquidus temperature than that of the higher extent melt (G2). The liquidus of the G2 clinopyroxene-free composition is lower (1360 °C) than that of G1 (1455 °C). Therefore, a multi-stage fractional melting of a progressively depleted source mantle cannot explain the difference between the two compositions.

The production of the contrasting compositions G1 and G2 requires <10 kbar partial melting of two different sources: a lherzolite for G1 and a harzburgite for G2. A process that might lead to the observed compositional dichotomy is the two-stage magma ocean solidification process that has been proposed for Mercury by Brown and Elkins-Tanton (2009). In this model a global magma ocean is produced by the energy of accretion and core formation. Solidification of this magma ocean proceeds in two major phases. The first stage is magma ocean crystallization from the core–mantle boundary to the surface of the planet (Solomatov, 2000). As crystals grow from the cooling magma, they preferentially incorporate Mg over Fe and sink to the bottom. This causes the residual melt to become iron-enriched and later-forming crystals become progressively enriched in Fe. This leads to a layered structure of the mantle and to density instability of the cumulate pile (e.g. Hess and Parmentier, 1995; Elkins-Tanton et al., 2003). The cumulate sequence then overturns just after magma ocean solidification ends in order to achieve a stable configuration. However, the low FeO magma ocean of Mercury might not have overturned because of the slightness of the density gradient within the cumulate pile (Brown and Elkins-Tanton, 2009; Riner et al., 2010). But, even without density instability, the thin (300–400 km) mantle of Mercury (Smith et al., 2012) will, for a range of structures, convect for much of

Mercury's history. Melt production can thus persist for periods ranging from 1 Ga and longer (Michel et al., 2012). During this process, lower density cumulates formed at the bottom of the pile rise buoyantly and undergo adiabatic decompression melting, producing partial melting of cumulates from the interior. Furthermore, if a flotation crust of less dense minerals has not formed during magma ocean solidification, the oldest crust of the planet would consist of the last dregs of the compositionally evolved magma ocean residual melts that solidified at the surface.

The final solidified crust and a remelt of early cumulates might explain the dichotomy between compositions G1 and G2. Most crystallization models presented by Brown and Elkins-Tanton (2009) for the crystallization of the mercurian magma ocean produce early cumulates that consist of olivine + low-Ca pyroxene. In the second stage during overturn, these less dense cumulates rise to shallow depth in Mercury (150 km depth to the surface) and undergo partial melting. The G2 composition could be a melt that was produced by this process, potentially followed by a small amount of fractional crystallization before eruption that allowed the composition to move off the olivine–protoenstatite peritectic and crystallize protoenstatite. The G1 composition would then represent a partial melt of solidified lherzolitic magma ocean cumulates.

6. Conclusions

This study is a first attempt to explore the significance of the major element compositional dichotomy observed in lavas from the surface of Mercury. Much more data will be made available in the near future by MESSENGER during its extended mission and, in coming years, by the BepiColombo mission (Rothery et al., 2010). Measurements on more specific areas should facilitate a better understanding of the relationships between surface composition and the different lithologies and geological terrains. More data will also assist in the identification of the speciation and distribution of sulfide. For example, the correlation between sulfide and calcium (Nittler et al., 2011; Weider et al., 2012) needs more detailed study.

In this contribution, we have identified the crystallization sequence of lavas of Mercury. The potential mineralogy of lavas at the surface is dominated by low-Ca pyroxenes (protoenstatite and orthoenstatite), plagioclase, trydimite, high-Ca pyroxene (augite) in some area and minor olivine if any. Two compositional groups have been discriminated and cannot be related by crystallization processes. While additional observations may result in a broadened compositional range, the primary conclusion here indicating unrelated origins should remain robust. This diversity suggests the existence of different sources, implying differentiation of the silicate portion of Mercury. Magma ocean crystallization forming a layered structure of the mantle followed by overturn/convection would produce adequate conditions to favor adabiatic decompression and partial melting of different mantle source, responsible for the compositional dichotomy at the surface of Mercury.

Acknowledgments

BC acknowledges support by a Marie Curie International Outgoing Fellowship within the 7th European Community Framework Programme. TLG is supported by NASA Cosmochemistry Grant NNX12AH80G. MTZ is supported by the NASA MESSENGER mission. Comments by Larry Nittler and careful reviews by Francis McCubbin and David Rothery improved the manuscript.

Appendix A. Supplementary meterials

Supplementary data associated with this article can be found in the online version at http://dx.doi.org/10.1016/j.epsl.2012.12.021.

References

Aitken, B.G., Echeverría, L.M., 1984. Petrology and geochemistry of komatiites and tholeiites from Gorgona Island, Colombia. Contrib. Mineral. Petrol. 86, 94–105.
Andersen, O., 1915. The system anorthite-forsterite-silica. Am. J. Sci. 39, 407–454.
Armstrong, J.T., 1995. Citzaf—a package of correction programs for the quantitative electron microbeam X-ray analysis of thick polished materials, thin-films, and particles. Microbeam Anal. 4, 177–200.
Arndt, N.T., Nisbet, E.G., 1982. Komatiites. George Allen and Unwin, London pp. 526.
Berthet, S., Malavergne, V., Righter, K., 2009. Melting of the Indarch meteorite (EH4 chondrite) at 1 GPa and variable oxygen fugacity: implications for early planetary differentiation processes. Geochim. Cosmochim. Acta 73, 6402–6420.
Blewett, D.T., Lucey, P.G., Hawke, B.R., Ling, G.G., Robinson, M.S., 1997. A comparison of mercurian reflectance and spectral quantities with those of the Moon. Icarus 129, 217–231.
Brown, S.M., Elkins-Tanton, L.T., 2009. Compositions of Mercury's earliest crust from magma ocean models. Earth Planet. Sci. Lett. 286, 446–455.
Corgne, A., Keshav, S., Wood, B.J., McDonough, W.F., Fei, Y., 2008. Metal–silicate partitioning and constraints on core composition and oxygen fugacity during Earth accretion. Geochim. Cosmochim. Acta 72, 574–589.
De Wit, M.J., Ashwal, L.D., 1997. Convergence towards divergent models of greenstone belts. Greenstone Belts. In: de Wit, M., Ashwall, L.D. (Eds.), Oxford Monograph on Geology and Geophysics, vol. 35. Oxford University Press, pp. ix–xvii.
Delano, J.W., 1986. Pristine lunar glasses: criteria, data, and implications. J. Geophys. Res. 91, D201–D213.
Denevi, B.W., et al., 2009. The evolution of Mercury's crust: a global perspective from MESSENGER. Science 324, 613–618.
Elkins-Tanton, L.T., Parmentier, E.M., Hess, P.C., 2003. Magma ocean fractional crystallization and cumulate overturn in terrestrial planets: implications for Mars. Meteorit. Planet. Sci. 38, 1753–1771.
Evans, L.G., et al., 2012. Major-element abundances on the surface of Mercury: results from the MESSENGER Gamma-Ray Spectrometer. J. Geophys. Res. 117, E00L07.
Fan, J., Kerrich, R., 1997. Geochemical characteristics of aluminum depleted and undepleted komatiites and HREE-enriched low-Ti tholeiites, western Abitibi greenstone belt: a heterogeneous mantle plume-convergent margin environment. Geochim. Cosmochim. Acta 61, 4723–4744.
Fassett, C.I., Kadish, S.J., Head, J.W., Solomon, S.C., Strom, R.G., 2011. The global population of large craters on Mercury and comparison with the Moon. Geophys. Res. Lett. 38, L10202.
Fassett, C.I., et al., 2012. Large impact basins on Mercury: global distribution, characteristics, and modification history from MESSENGER orbital data. J. Geophys. Res. 117, E00L08.
Filiberto, J., Dasgupta, R., 2011. Fe^{2+}–Mg partitioning between olivine and basaltic melts: applications to genesis of olivine-phyric shergottites and conditions of melting in the Martian interior. Earth Planet. Sci. Lett. 304, 527–537.
Giordano, D., Russell, J.K., Dingwell, D.B., 2008. Viscosity of magmatic liquids: a model. Earth Planet. Sci. Lett. 271, 123–134.
Grove, T.L., 1981. Use of FePt alloys to eliminate the iron loss problem in 1 atm gas mixing experiments: theoretical and practical considerations. Contrib. Mineral. Petrol. 78, 298–304.
Grove, T.L., 1993. Corrections to expressions for calculating mineral components in "Origin of calc-alkaline series lavas at medicine lake volcano by fractionation, assimilation and mixing" and "Experimental petrology of normal MORB near the kane fracture zone: 22°–25°N, mid-atlantic ridge". Contrib. Mineral. Petrol. 114, 422–424.
Grove, T.L., Parman, S.W., 2004. Thermal evolution of the Earth as recorded by komatiites. Earth Planet. Sci. Lett. 219, 173–187.
Gudfinnsson, G.H., Presnall, D.C., 2000. Melting behaviour of model lherzolite in the system CaO–MgO–Al_2O_3–SiO_2–FeO at 0.7–2.8 GPa. J. Petrol. 41, 1241–1269.
Head, J.W., et al., 2011. Flood volcanism in the northern high latitudes of Mercury revealed by MESSENGER. Science 333, 1853–1856.
Head, J.W., et al., 2008. Volcanism on Mercury: evidence from the first MESSENGER flyby. Science 321, 69–72.
Hess, P.C., Parmentier, E.M., 1995. A model for the thermal and chemical evolution of the Moon's interior: implications for the onset of mare volcanism. Earth Planet. Sci. Lett. 134, 501–514.
Hollings, P., Kerrich, R., 1999. Trace element systematics of ultramafic and mafic volcanic rocks from the 3 Ga North Caribou greenstone belt, northwestern Superior Province. Precambrian Res. 93, 257–279.
Keil, K., 1968. Mineralogical and chemical relationships among enstatite chondrites. J. Geophys. Res. 73, 6945–6976.
Kerber, L., et al., 2011. The global distribution of pyroclastic deposits on Mercury: the view from MESSENGER flybys 1–3. Planet. Space Sci. 59, 1895–1909.

Kushiro, I., 1972. Determination of liquidus relations in synthetic silicate systems with electron probe analysis: the system forsterite–diopside–silica at 1 atm. Am. Mineral. 57, 1260–1271.
Larimer, J.W., Ganapathy, R., 1987. The trace element chemistry of CaS in enstatite chondrites and some implications regarding its origin. Earth Planet. Sci. Lett. 84, 123–134.
Lawrence, D.J., et al., 2010. Identification and measurement of neutron-absorbing elements on Mercury's surface. Icarus 209, 195–209.
Le Bas, M.J., 2000. IUGS reclassification of the high-Mg and picritic volcanic rocks. J. Petrol. 41, 1467–1470.
Li, J., Agee, C.B., 1996. Geochemistry of mantle-core differentiation at high pressure. Nature 381, 686–689.
Liu, T.-C., Presnall, D.C., 1990. Liquidus phase relationships on the join anorthite-forsterite-quartz at 20 kbar with applications to basalt petrogenesis and igneous sapphirine. Contrib. Mineral. Petrol. 104, 735–742.
Longhi, J., Boudreau, A.E., 1980. The orthoenstatite liquidus field in the system forsterite-diopside-silica at one atmosphere. Am. Mineral. 65, 563–573.
Longhi, J., Pan, V., 1988. A reconnaisance study of phase boundaries in low-alkali basaltic liquids. J. Petrol. 29, 115–147.
Malavergne, V., Toplis, M.J., Berthet, S., Jones, J., 2010. Highly reducing conditions during core formation on Mercury: implications for internal structure and the origin of a magnetic field. Icarus 206, 199–209.
McClintock, W.E., et al., 2008. Spectroscopic observations of Mercury's surface reflectance during MESSENGER's first Mercury flyby. Science 321, 62–65.
McCoy, T.J., Dickinson, T.L., Lofgren, G.E., 1999. Partial melting of the Indarch (EH4) meteorite: a textural, chemical, and phase relations view of melting and melt migration. Meteorit. Planet. Sci. 34, 735–746.
McCubbin, F.M., Riner, M.A., Vander Kaaden, K.E., Burkemper, L.K., 2012. Is Mercury a volatile-rich planet? Geophys. Res. Lett. 39, L09202.
Michel N.C., Hauck II S.A., Solomon S.C., Phillips R.J., Roberts J.H., Zuber M.T., 2012. Implications of MESSENGER observations for mantle convection of Mercury. In: Proceedings of the 43rd Lunar Planetary Science Conference, p.1671.
Nittler, L.R., et al., 2011. The major-element composition of Mercury's surface from MESSENGER x-ray spectrometry. Science 333, 1847–1850.
Osborn, E.F., Tait, D.B., 1952. The system diopside–forsterite–anorthite. Am. J. Sci. Bowen Volume, 413–433.
Papike, J.J., Ryder, G., Shearer, C.K., 1998. Lunar samples. Rev. Mineral. Geochem. 36 (5.1–5), 234.
Parman, S.W., Grove, T.L., Dann, J.C., 2001. The production of Barberton komatiites in an Archean subduction sone. Geophys. Res. Lett. 28, 2513–2516.
Peplowski, P.N., et al., 2011. Radioactive elements on Mercury's surface from MESSENGER: implications for the planet's formation and evolution. Science 333, 1850–1852.
Polat, A., Kerrich, R., Wyman, D.A., 1999. Geochemical diversity in oceanic komatiites and basalts from the late Archean Wawa greenstone belts, Superior Province, Canada: trace element and Nd isotope evidence for a heterogeneous mantle. Precambrian Res. 94, 139–173.
Presnall, D.C., et al., 1978. Liquidus phase relations on the join diopside-forsterite-anorthite from 1 atm to 20 kbar: their bearing on the generation and crystallization of basaltic magma. Contrib. Mineral. Petrol. 66, 203–220.
Presnall, D.C., Dixon, J.R., O'Donnell, T.H., Dixon, S.A., 1979. Generation of mid-ocean ridge tholeiites. J. Petrol. 20, 3–35.
Prockter, L.M., et al., 2010. Evidence for young volcanism on Mercury from the third MESSENGER flyby. Science 329, 668–671.
Rava, B., Hapke, B., 1987. An analysis of the Mariner 10 color ratio map of mercury. Icarus 71, 397–429.
Riner, M.A., Lucey, P.G., Desch, S.J., McCubbin, F.M., 2009. Nature of opaque components on Mercury: insights into a Mercurian magma ocean. Geophys. Res. Lett. 36, L02201.
Riner, M.A., McCubbin, F.M., Lucey, P.G., Talyor, G.J., Gillis-Davis, J.J., 2010. Mercury surface composition: integrating petrologic modeling and remote sensing data to place constraints on FeO abundance. Icarus 209, 301–313.
Riner, M.A., Lucey, P.G., McCubbin, F.M., Taylor, G.J., 2011. Constraints on Mercury's surface composition from MESSENGER neutron spectrometer data. Earth Planet. Sci. Lett. 308, 107–114.
Robinson, M.S., Lucey, P.G., 1997. Recalibrated Mariner 10 color mosaics: implications for Mercurian volcanism. Science 275, 197–200.
Robinson, M.S., et al., 2008. Reflectance and color variations on Mercury: regolith processes and compositional heterogeneity. Science 321, 66–69.
Rothery, D., et al., 2010. Mercury's surface and composition to be studied by BepiColombo. Planet. Space Sci. 58, 21–39.
Schlemm, C., et al., 2007. The X-Ray spectrometer on the MESSENGER spacecraft. Space Sci. Rev. 131, 393–415.
Sen, G., Presnall, D.C., 1984. Liquidus phase relationships on the join anorthite–forsterite–quartz at 10 kbar with applications to basalt petrogenesis. Contrib. Mineral. Petrol. 85, 404–408.
Smith, J.V., 1969. Crystal structure and stability of the $MgSiO_3$ polymorphs: physical properties and phase relations of Mg,Fe pyroxenes. Miner. Soc. Amr. Spec. Paper 2, 3–29.
Smith, D.E., Zuber, M.T., Phillips, R.J., Solomon, S.C., Hauck, S.A., Lemoine, F.G., Mazarico, E., Neumann, G.A., Peale, S.J., Margot, J.-L., Johnson, C.L., Torrence, M.H., Perry, M.E., Rowlands, D.D., Goossens, S., Head, J.W., Taylor, A.H., 2012. Gravity field and internal structure of Mercury from MESSENGER. Science 336, 214–217.
Solomatov, V.S., 2000. Fluid dynamics of a terrestrial magma ocean. In: Canup, R.M., Righter, K. (Eds.), Origin of the Earth and Moon. University of Arizona Press, Phoenix, pp. 323–338.
Sprague, A.L., et al., 2009. Spectral emissivity measurements of Mercury's surface indicate Mg- and Ca-rich mineralogy, K-spar, Na-rich plagioclase, rutile, with possible perovskite, and garnet. Planet. Space Sci. 57, 364–383.
Strom, R.G., Trask, N.J., Guest, J.E., 1975. Tectonism and volcanism on Mercury. J. Geophys. Res. 80, 2478–2507.
Taylor, G.J., Scott, E.R.D., 2003. Mercury. In: Heinrich, D.H., Karl, K.T. (Eds.), Treatise on Geochemistry. Pergamon, Oxford, pp. 477–485.
Viljoen, M.J., Viljoen, R.P., 1969. The geology and geochemistry of the lower ultramafic unit of the Onverwacht Group and a proposed new class of igneous rocks. Geol. Soc. S. Afr. Spec. Publ. 2, 55–86.
Wadhwa, M., 2008. Redox conditions on small bodies, the Moon and Mars. Rev. Mineral. Geochem. 68, 493–510.
Weng, Y.-H., Presnall, D.C., 2001. The system diopside–forsterite–enstatite at 5.1 GPa: a ternary model for melting of the mantle. Can. Mineral. 39, 299–308.
Wasson, J.T., 1988. The building stones of the planets. In: Vilas, F., Chapman, C.R., Matthews, M.S. (Eds.), Mercury. The University of Arizona Press, Tucson, pp. 622–650.
Weider, S.Z., Nittler, L.R., Starr, R.D., McCoy, T.J., Stockstill-Cahill, K.R., Byrne, P.K., Denevi, B.W., Head, J.W., Solomon, S.C., 2012. Chemical heterogeneity on Mercury's surface revealed by the MESSENGER X-Ray Spectrometer. J. Geophys. Res. 117, E00L05.
Yasuda, M., Kitamura, M., Morimoto, N., 1983. Electron microscopy of clinoenstatite from a boninite and a chondrite. Phys. Chem. Miner. 9, 192–196.
Yoder, H.S., 1976. Generation of Basaltic Magma. National Academy of Science, Washington, DC, p. 278.
Zolotov, M.Y., 2011. On the chemistry of mantle and magmatic volatiles on Mercury. Icarus 212, 24–41.